This is a repository copy of *An extension of mean-field coarsening theory to include particle coalescence using nearest-neighbour functions*.

An extension of mean-field coarsening theory to include particle coalescence using nearest-neighbour functions

Hector Basoalto and Magnus Anderson*

School of Metallurgy and Materials, University of Birmingham, Edgbaston, Birmingham B15 2TT, UK

Abstract

A mean field description of particle coalescence and Ostwald ripening is presented. The inclusion of particle coalescence events is shown to influence the evolution of the size distribution function and the time taken to reach the steady state particle coarsening regime. Nearest neighbour functions are used to represent the spatial arrangement of particles within multi-modal particle radius distributions and to calculate the frequency of coalescence events. The impact of particle coalescence upon long term coarsening kinetics has been studied. By tracking the evolution of a unimodal and bimodal dispersions in phase space, it is demonstrated that coalescence affects the paths of particle dispersion towards the steady state particle coarsening regime as well as the time scales to reach it.

Keywords: multimodal γ' dispersion, mean field theory, coalescence, Nickel-based superalloys

1. Introduction

The mechanical response of precipitate strengthened alloys are significantly influenced by the size and spatial distribution of the embedded particle phase. At high temperatures the dispersion is unstable, with particle growth rates driven by the minimisation of the free energy. During Oswald ripening, kinetics of particle coarsening are driven by the minimisation of the interfacial energy between the particle and matrix phases. This phenomena was first treated by Greenwood [1] and later expanded into a comprehensive mean field theory by Lifshitz and Slyozov [2] and Wagner [3] (LSW) for dilute particle dispersions in a binary alloy. LSW coarsening theory predicts the existence of an attractor (steady) state for the particle radius distribution. Once such a state is attained LSW theory predicts scaling laws for the temporal evolution of the moments of the particle size distribution: the cubed mean particle radius increases linearly with time and the concentration of particles decreases linearly with time.

Over the last forty to fifty years, there has been a considerable effort on the extension of LSW coarsening theory to describe particle kinetics in engineering precipitate strengthened materials. Progress has been made in linking the chemical composition of alloys to coarsening ki-

---

*Corresponding author
   Email address: h.basoalto@bham.ac.uk, m.j.anderson@bham.ac.uk ()

netics through CALPHAD (Computer Coupling of Phase Diagrams and Thermochemistry) [4]. Kheuman and Voorhees [5] developed a description of ternary alloys, which was later generalised to multi-components by Jou *et al.* [6] and Phillipe and Voorhees [7]. Other multi-component formulations have been developed such as that by Svoboda *et al.* [8] and Chen *et al.* [9]. Software such as TC PRISMA [10] and MatCalc [11] offer the ability to calculate the phase diagram, particle composition, thermodynamic variables and mobility variables needed to determine the particle kinetics as a function of chemical composition. These models capture the formation and growth of particles, describing Ostwald ripening kinetics coupled with classical nucleation theory.

Another key aspect in simulating the precipitate kinetics in engineering alloys is the treatment of non-dilute particle systems [12]. Neighbouring particle's diffusion fields may interact, accelerating the particle growth or dissolution rate. Multiple-particle diffusion has been assessed by describing the diffusion field as quasi-static with particles treated as either point sources or sinks [13, 14, 15]. Several authors have built upon this approach and that of Ardell [12], deriving correction factors to modify dilute particle growth rates to describe finite volume fraction particle dispersions [16, 17, 18].

Other phenomena may impact particle coarsening behaviour such as changes in particle morphology [19, 20], inverse coarsening [21] and particle coalescence [22]. Differences in lattice parameter between coherent particles and matrix gives rise to misfit stresses which contribute to the elastic strain energy and influences the particle morphology [19]. When the contribution to the total energy of elastic strain energy is greater than that of interfacial energy, it is possible that small particles grow at the expense of larger particles. Su *et al.* [21] describe such events as inverse coarsening. In high volume fraction particle dispersions, particle coalescence can impact both particle morphology and size [22].

The aim of this paper is to further develop the mean field description of population dynamics of polydispersed particles to include coalescence events. The approach involves introducing appropriate coalescence source and sink terms to the advection differential equation governing the evolution of the particle size distribution and is developed in Section 2. To account for the spatial arrangement of particles, a statistical approach based on nearest neighbour functions has been adopted. Numerical implementation of the model is outlined in Section 3. The results and discussion sections are given in Sections 4 and 5, and the work is concluded in Section 6.

2. A mean field description of particle coarsening and coalescence

2.1. Evolution of the particle radius distribution

The particle radius distribution function $F(R, t)$ is defined as follows: the number of particles per unit volume with radius between R and $R + dR$ is given by $F(R, t)dR$. The total number of

particles per unit volume $N_v(t)$ is then the integral of this function for all possible particle radii

$$N_v(t) = \int_0^\infty F(R,t)\, dR \tag{1}$$

Nucleation, dissolution and coalescence of particles will influence the temporal evolution of $N_v(t)$. These mechanisms can be accounted for by introducing appropriate source and sink terms, such that the rate of change of the total number of particles per unit volume is given by

$$\dot{N}_v(t) = \dot{N}_v^+(t) - \dot{N}_v^-(t) \tag{2}$$

where $\dot{N}_v^+(t)$ and $\dot{N}_v^-(t)$ are the 'generation' and 'removal' rates, respectively. These are associated with a number of possible phenomena such as nucleation, coalescence and dissolution. Both $\dot{N}_v^+(t)$ and $\dot{N}_v^-(t)$ can be expressed in terms of particle size density functions $\dot{n}^+(R,t)$ and $\dot{n}^-(R,t)$, so that the number of particles generated and removed per unit volume with radius lying in the closed interval $[R, R+dR]$ is then $d\dot{N}^+ = \dot{n}^+(R,t)dR$ and $d\dot{N}^- = \dot{n}^-(R,t)dR$. With these definitions, Equation (2) becomes

$$\dot{N}_v(t) = \int_0^\infty \left(\dot{n}^+(R,t) - \dot{n}^-(R,t) \right) dR \tag{3}$$

The source terms $\dot{n}^+(R,t)$ and $\dot{n}^-(R,t)$ may be introduced into the continuity equation:

$$\frac{\partial F(R,t)}{\partial t} + \frac{\partial (F(R,t)\, V(R,t))}{\partial R} = \dot{n}^+(R,t) - \dot{n}^-(R,t) \tag{4}$$

From the moments of $F(R,t)$ the mean particle size and volume fraction of the dispersion can be calculated:

$$\langle R \rangle = \frac{1}{N_v} \int_0^\infty R\, F(R,t) dR \tag{5}$$

$$\phi = \frac{4}{3}\pi \int_0^\infty R^3 F(R,t) dR \tag{6}$$

The general form of the particle growth rate for spherical particles is given by [23]

$$V(R,t) = \frac{A(t)}{R} \left(\frac{1}{R_c(t)} - \frac{1}{R} \right) z(R,t) \tag{7}$$

where A is a function of the diffusivities of the alloying elements. The term z is a correction factor that accounts for competitive growth [12, 13, 14, 16, 15, 17, 18]. The parameter R_c is a critical radius and represents the particle size at which the transition between dissolution and growth occurs. The mean field description outlined above assumes that particles are spherical and maintain this morphology as the particle radius distribution evolves.

2.2. Particle coalescence

Consider the coalescence of two particles of size R_1 and R_2 forming a new particle of size R. Introducing the volume fraction frequency density $g(R,t)$ defined such that the volume fraction of particles having radius between R and $R + dR$ is $g(R,t)dR$. This is the probability of finding

3

particles with radius lying in the closed interval $[R, R + dR]$. It is related to the distribution function $F(R, t)$ as follows

$$g(R, t)dR = \frac{4\pi}{3} F(R, t)R^3 dR \tag{8}$$

Assuming that the probability of any two particles randomly sampled from the dispersion having sizes R_1 and R_2 are independent from each other, then the likelihood of the first particle having a radius $R_1 \in [R_1, R_1 + dR_1]$ and the second particle having a radius in $R_2 \in [R_2, R_2 + dR_2]$ is given by $g(R_1, t), g(R_2, t)dR_1 dR_2$. Let $G_p(R_1, R_2, \lambda)$ be a spatial distribution function (to be defined in Section 2.3) such that the probability of finding a particle of size R_1 at a distance $[\lambda, \lambda + d\lambda]$ from R_2 is given by $G_p(R_1, R_2, \lambda)d\lambda$. The probability of two particles with radius $R_1 \in [R'_1, R'_1 + dR'_1]$ and $R_2 \in [R'_2, R'_2 + dR'_2]$ a distance $\lambda \in [\lambda', \lambda' + d\lambda']$ is

$$P\left[R'_1 < R_1 \leq R'_1 + dR'_1, R'_2 < R_2 \leq R'_2 + dR'_2, \lambda' < \lambda \leq \lambda' + d\lambda'\right] = f_c\left(R'_1, R'_2, \lambda'\right) dR'_1 dR'_2 d\lambda' \tag{9}$$

where

$$f_c\left(R'_1, R'_2, \lambda'\right) = g(R'_1, t)\, g(R'_2, t)\, G_p(R'_1, R'_2, \lambda') \tag{10}$$

If at any given time only two particles merge, the total possible number of coalesce events is $1/2\, N_v$. The particle collide a rate is then given by $1/2\, N_v\, \Gamma(R_1, R_2, \lambda)\, f_c\left(R'_1, R'_2, \lambda'\right) dR'_1 dR'_2 d\lambda'$, where $\Gamma(R_1, R_2, \lambda)$ is the frequency at which two particles R_1 and R_2 initially a distance λ apart coalesce. Integrating over all possible values of R_1, R_2 and λ, the rate of coalescence is given by

$$\dot{N}_v^+(t) = \frac{1}{2} N_v(t) \int_0^\infty \int_0^\infty \int_0^\infty \Gamma\left(R'_1, R'_2, \lambda'\right)\, f_c\left(R'_1, R'_2, \lambda'\right) dR'_2\, d\lambda'\, dR'_1 \tag{11}$$

Since the integral is identified as the expectation value of the coalescence frequency $\langle \Gamma \rangle$, it follows that Equation (11) can be expressed as $\dot{N}_v^+ = 1/2\, N_v\, \langle \Gamma \rangle$. Carrying out a change of variable from R'_1 to R using the volume constraint $R^3 = R'^3_1 + R'^3_2$, Equation (11) becomes

$$\dot{N}_v^+(t) = \frac{1}{2} N_v(t) \int_0^\infty \int_0^\infty \int_0^\infty \frac{R^2\, \Gamma\left((R^3 - R_2^3)^{1/3}, R'_2, \lambda'\right)\, f_c\left((R^3 - R_2^3)^{1/3}, R'_2, \lambda'\right)}{(R^3 - R'^3_2)^{2/3}}\, dR'_2\, d\lambda'\, dR \tag{12}$$

Comparing Equations (11)with (3) we obtain the following expression for the generation rate density function

$$\dot{n}_v^+(R, t) = \frac{1}{2} N_v(t) \int_0^\infty \int_0^\infty \frac{R^2\, \Gamma\left((R^3 - R_2^3)^{1/3}, R'_2, \lambda'\right)\, f_c\left((R^3 - R_2^3)^{1/3}, R'_2, \lambda'\right)}{(R^3 - R'^3_2)^{2/3}}\, dR'_2\, d\lambda' \tag{13}$$

The particle sink rate $\dot{n}_v^-(R, t)$ can be derived by considering the frequency at which a particle of size R is intercepted by another of size R'. Using similar arguments as above, the rate at which particles are removed due to collision is given by

$$\dot{n}_v^-(R, t) = N_v(t) \int_0^\infty \int_0^\infty \Gamma\left(R, R', \lambda'\right)\, f\left(R, R', \lambda'\right)\, dR'\, d\lambda' \tag{14}$$

The frequency of coalescence, $\Gamma(R_1, R_2, \lambda)$ can be determined from the inverse of the time taken for two particles to grow such that their separation distance $\lambda \to 0$. This occurs at a rate given

4

by

$$\frac{d\lambda(R_1, R_2)}{dt} = -\left[V(R_1, t) + V(R_2, t)\right] \tag{15}$$

where the growth rates of the two particles are given by $V(R_1, t)$ and $V(R_2, t)$ respectively. It is currently assumed that the particles are spherical. In real alloys the precipitate morphologies can have complex shapes and the mean interface velocity of such particles will deviate from that of a sphere. In particular, in high volume fraction nickel-based superalloys, large γ' particles tend to be cuboidal and in this case they will grow at a slower rate than that predicted for a spherical particle of equivalent volume due to its planar interfaces. As a result, the mean growth rate of a particle, $\bar{V}$ may be related to the growth rate a spherical particle of equivalent volume through the following relation, $V(R, t) = k\bar{V}(R, t)$, where k is a scaling parameter associated with the ratio of area of curved surfaces and total surface area of the particle. Solving the Equation (15) for the time t^* as $\lambda \to 0$, the coalescence rate can then be estimated through the relation

$$\Gamma\left(R_1, R_2, \lambda\right) = \frac{k}{t^*} s(t - t^*) \tag{16}$$

where $s(t - t^*) = 1$ if $t > t^*$ and $s(t - t^*) = 0$ if $t < t^*$.

2.3. Nearest neighbour functions

The coalescence rates derived in the previous section require knowledge of the spatial distribution function $G_p(R_1, R_2, \lambda)$. Lu and Torquato [24] have developed spatial probability functions descriptive of the particle spacing in systems of randomly dispersed penetrable or impenetrable spheres. This work makes use of the nearest neighbour functions descriptive of three dimensional impenetrable spheres [25, 26].

Consider a poly-dispersion of particles. Figure 1 gives a schematic representation of the parameters used to define the spatial arrangement. Surrounding each particle is a spherical domain Ω that is free of neighbouring particles. Torquato [25] defines the exclusion probability, $E_p(R, \lambda^*)$, as the likelihood of finding a region Ω of radius λ^* enclosing a particle of radius R. The interparticle spacing between the reference particle and the nearest neighbour is given by λ. The dependence of $E_p(R, \lambda^*)$ on λ^* is illustrated in Figure 2(a). For values of λ^* less than the radius R we have $E_p(R, \lambda^*) = 1$. For $\lambda^* > R$ the likelihood of encountering a neighbouring particle increases and thus E_p decreases. The distance at which $E_p \to 0$ is the maximum possible distance between the centre of the particles of radius R and the nearest neighbouring particle's surface predicted by the E_p function.

Let $H_p(R, \lambda^*)$ be a probability density function such that the likelihood of finding a nearest neighbour at a distance within the closed interval $[\lambda^*, \lambda^* + d\lambda^*]$ from the reference particle centre
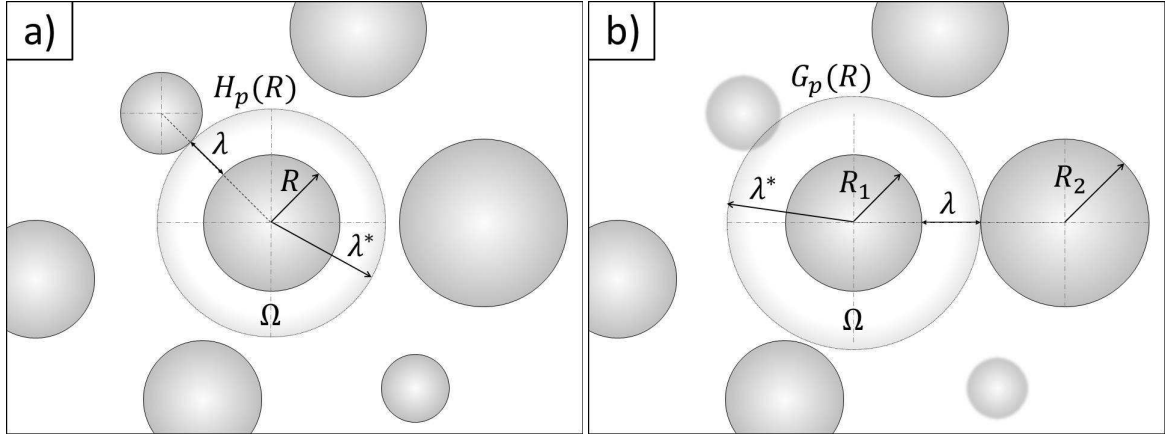
5

Figure 1: An illustration of the nearest neighbour function a) $H_p(R)$ and b), $G_p(R_1, R_2)$.

is $H_p(R, \lambda^*)d\lambda^*$. The $H_p(R, \lambda^*)$ function is related to $E_p(R, \lambda^*)$ through the relations [25]:

$$E_p(R, \lambda^*) = 1 - \int_0^{\lambda^*} H_p(x)dx$$

$$H_p(R, \lambda^*) = -\frac{\partial E_p}{\partial \lambda^*} \tag{17}$$

The $E_p(R, \lambda^*)$ and $H_p(R, \lambda^*)$ functions are obtained from the particle radius probability density function, $f(R, t) = F(R, t)/N_v(t)$. The $E_p(R, \lambda^*)$ function can be calculated from the moments of $f(R, t)$. The Dth moment is defined as

$$\langle R^D(t) \rangle = \int_0^{\infty} R^D f(R, t) \, dR \tag{18}$$

where D is the degree of the moment. The specific surface of the particle dispersion, S is given by

$$S = \frac{\langle R^2 \rangle}{\langle R^3 \rangle} \langle R \rangle \tag{19}$$

The calculation for the function $E_p(R, \lambda^*)$ is given in Equation set (20), where the radius of the spherical region Ω is normalised by the mean diameter of the particle radius distribution $(2\langle R \rangle)$ [24]:

$$x = \lambda^*/(2\langle R \rangle)$$

$$E_v(x) = \phi.exp\left[-2\phi S \left(a_0 x^3 + a_1 x^2 + a_2 x\right)\right]$$

$$E_p(x) = \frac{E_v(x)}{E_v(x = R/(2\langle R \rangle))}$$

$$H_p(x) = -\frac{\partial E_p}{\partial \lambda^*} = \frac{\phi S}{2\langle r \rangle} \left(3a_0 x^2 + 2a_1 x + a_2\right) E_p(x) \tag{20}$$

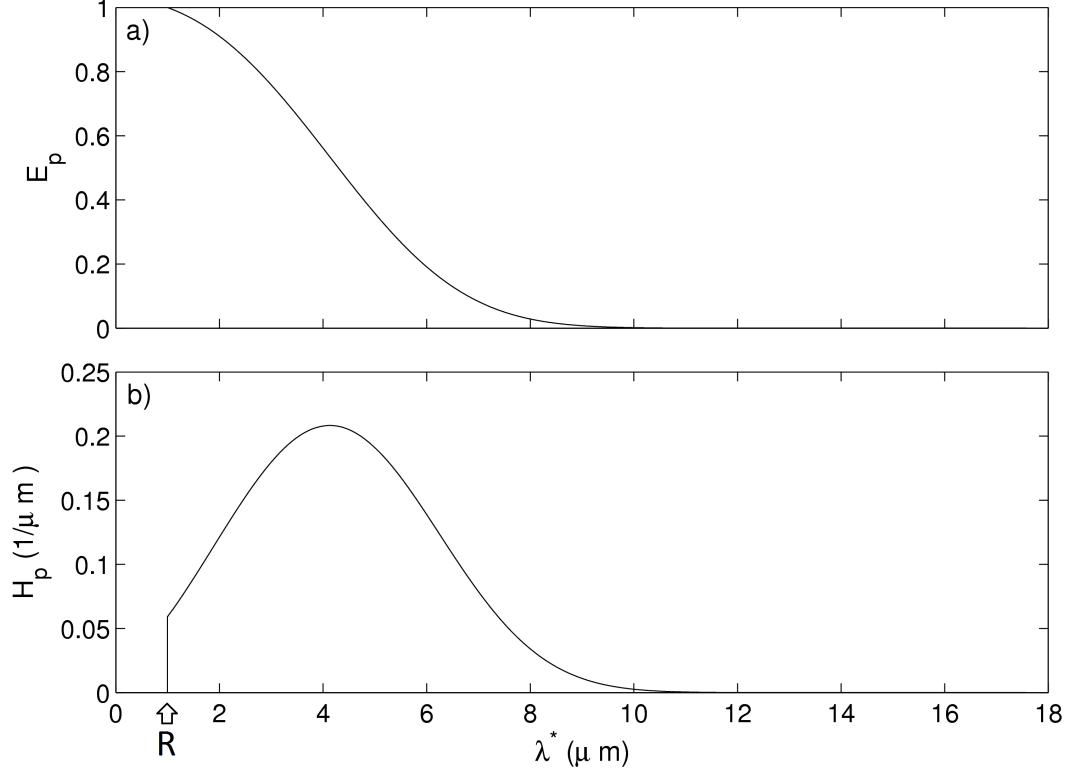$$E_p(\lambda^*) = 1, \quad H_p(\lambda^*) = 0, \quad for \, 0 \leq \lambda^* \leq R$$

6

Figure 2: An example of the E_p and H_p functions.

The coefficients a_0, a_1 and a_2 are

$$a_0 = \frac{4\left[\langle R\rangle^2/\langle R^2\rangle\right](1-\phi)(1-\eta+3\phi S)+8\phi^2 S^2}{(1-\phi)^3}$$

$$a_1 = \frac{6\left[\langle R\rangle^2/\langle R^2\rangle\right](1-\phi)+9\phi S}{(1-\phi)^2} \tag{21}$$

$$a_2 = \frac{1}{1-\phi}$$

The mean particle spacing for particles of radius R is

$$\bar{\lambda}(R) = \int_R^\infty E_p(R,\lambda^*)\,d\lambda^* = \int_0^\infty \lambda^* H_p(R,\lambda^*)\,d\lambda^* - R \tag{22}$$

To evaluate the accuracy of the nearest neighbour function method, a similar approach to the numerical analysis of Lu and Torquato [24] has been implemented and applied to a unimodal and bimodal distribution of particles. This involves generating randomly dispersed three dimensional systems of impenetrable spheres with periodic boundary conditions. The Gaussian and bimodal distributions described by Chen and Voorhees [27] have been used to define the initial shape of
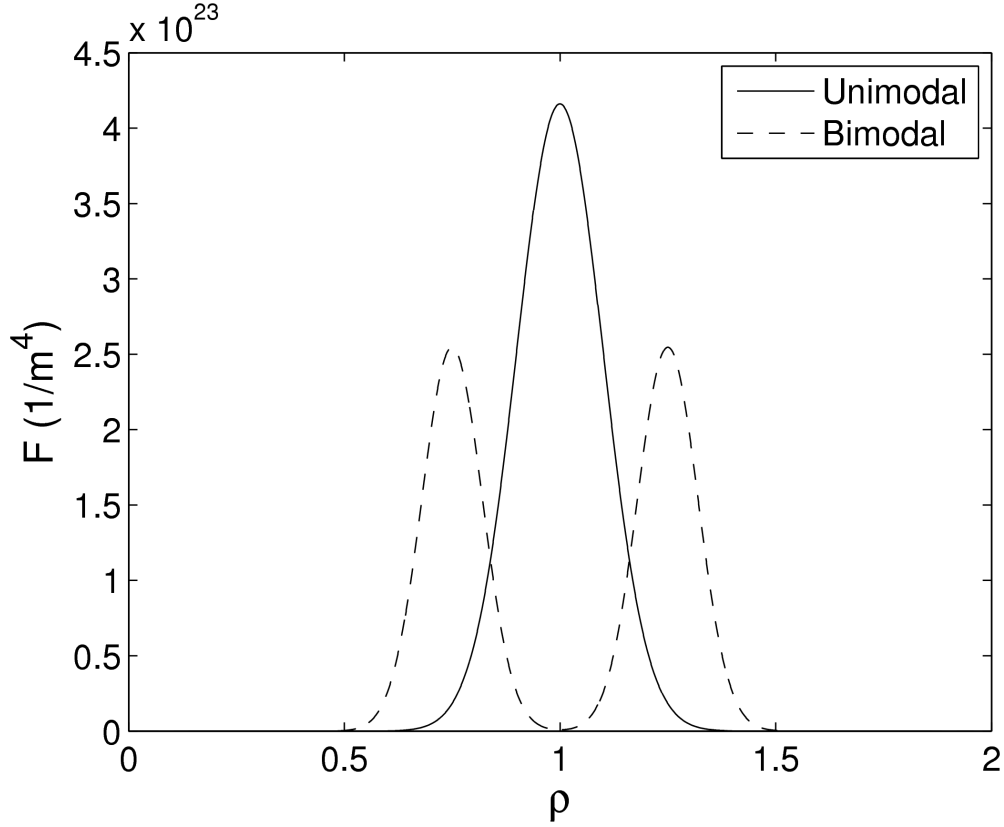
7

Figure 3: The initial particle radius distributions used in this study.

the particle radius distribution, and are given by

$$\chi(\rho, t = 0) = \frac{A}{\sigma\sqrt{2\pi}} exp\left[\frac{-(\rho - \mu)^2}{2\sigma^2}\right]$$

$$\rho = R(t)/\langle R(t)\rangle$$

$$\chi(\rho, t = 0)\, d\rho = \frac{4\pi}{\phi_\infty} F(R, t)\, \langle R(0)\rangle^3\, dR \qquad (23)$$

where μ and σ affect the shape of the size distribution and the normalisation constant A is determined from mass balance. These are illustrated in Figure 3. The unimodal particle radius distribution is generated using a μ parameter value of 1.0 and a σ value of 0.1. The bimodal distribution is generated using μ values of 0.75 and 1.25, and σ values of 0.07 and 0.25. Both particle radius distributions had a mean particle radius of $1\mu m$ with a volume fraction of 40%.

To generate systems of randomly dispersed non-penetrating spheres, an initial system of compact particles was created from the cumulative distribution function associated with $f(R, t)$. The method used to generate the initial structure was similar to that of Zhou *et. al.* [28], and is based on a rain dropping algorithm. Once a compact dispersion of particles was obtained, the next step was to repeatedly move each particle in a random direction by a small amount. The mean particle spacing was used to determine the amount of movement needed to obtain a
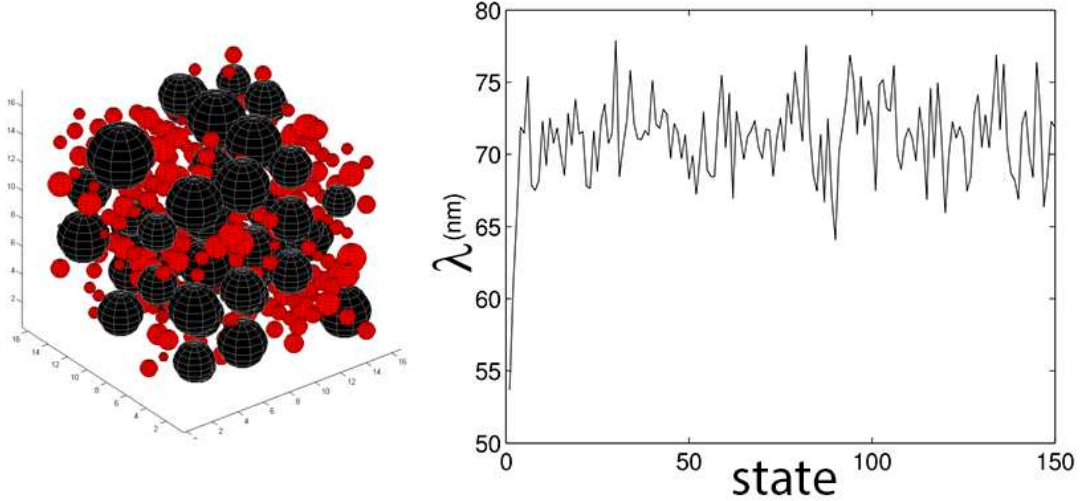
Figure 4: Generation of a random particle dispersion. (a) A bi-modal particle ensemble; (b) Change in mean particle spacing due to random movement of particles.

random dispersion, as shown in Figure 4. A total of 5956 and 8365 unique particles were used to describe the unimodal and bimodal particle radius distributions, respectively. Different spatial configurations of these particles were used to assess a total of 482,436 and 677,565 particles for the unimodal and bimodal distributions.

Figure 5 compares the mean particle spacing of a reference particle from the numerically generated data to the calculated mean spacing from Equation 22. The calculated and measured exclusion probabilities are compared in Figures 6 and 7, which show reasonable agreement. The variations (5%-95% percentile) in the numerically determined data are also shown in Figures 4-7. The mean relative difference between the mean spacings calculated using the $H_p(\lambda^*, R)$ function and the numerically generated particle systems is -9.04 $\pm$ 3.75 %. The difference is within the standard deviation of the particle spacings measured from the numerically generated particle systems.

Although it has been demonstrated that Equations (20 - 22) can be applied to bimodal particle distributions with reasonable accuracy, there is a limit to the width of the shape of the particle radius distribution that may be described. The issue occurs when $E_v(R, \lambda^*) \to 0$. This becomes a problem for particle radius distributions where the maximum particle radius is significantly greater than the mean particle radius, such as the tri-modal particle radius distributions that exist in turbine disc nickel-based superalloys. The method adopted in this work was to determine the largest particle size that can be calculated and restrict the reference particle size to a value below this limit.

When calculating the coalescence rates $\dot{n}_v^+(R, t)$ and $\dot{n}_v^-(R, t)$, the nearest neighbour function
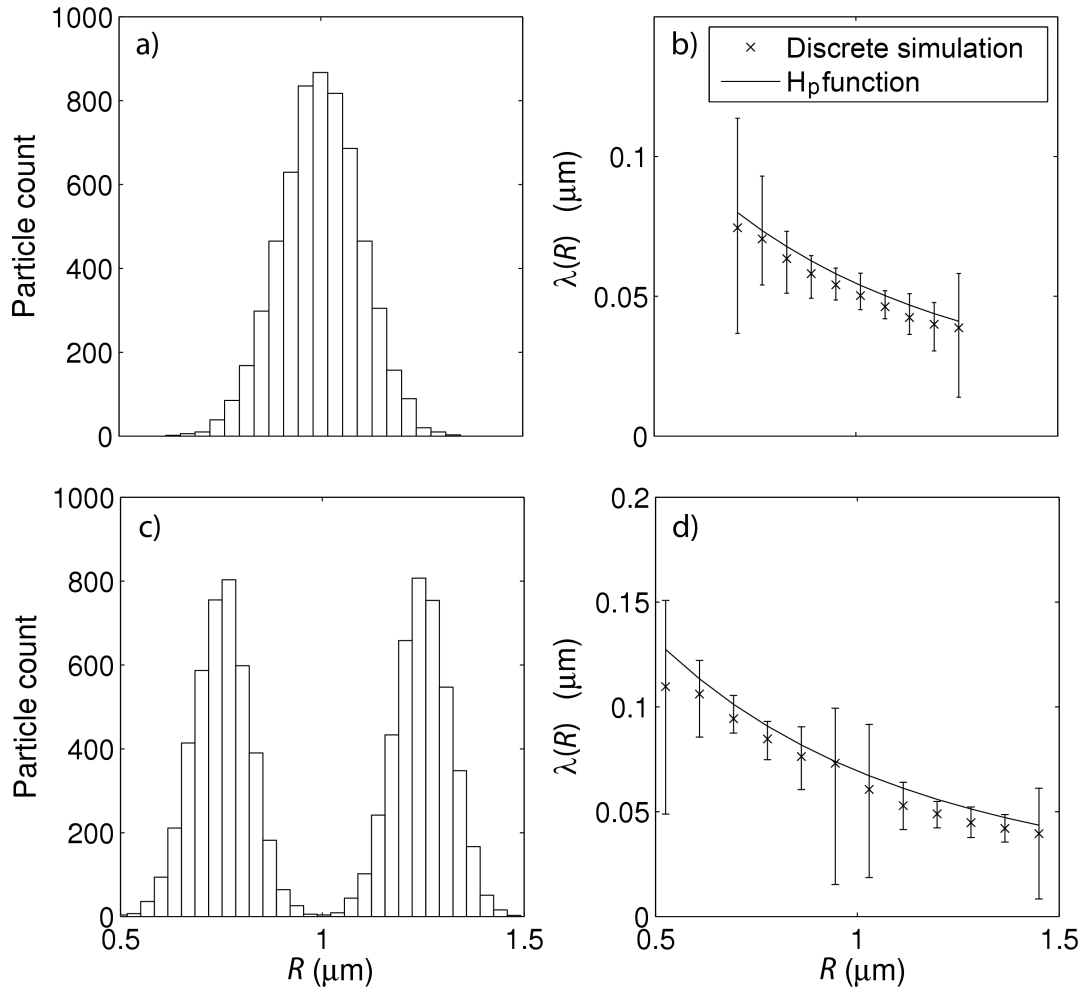
9

Figure 5: The comparison of the predicted and numerically measured particle spacing for different reference particles in the a) unimodal and b) bimodal particle radius distributions.

Figure 6: A comparison of the predicted exclusion probability and the exclusion probability measured from a unimodal distribution of particles created numerically. The black crosses refer to the numerically generated data whilst the red line describes the prediction.
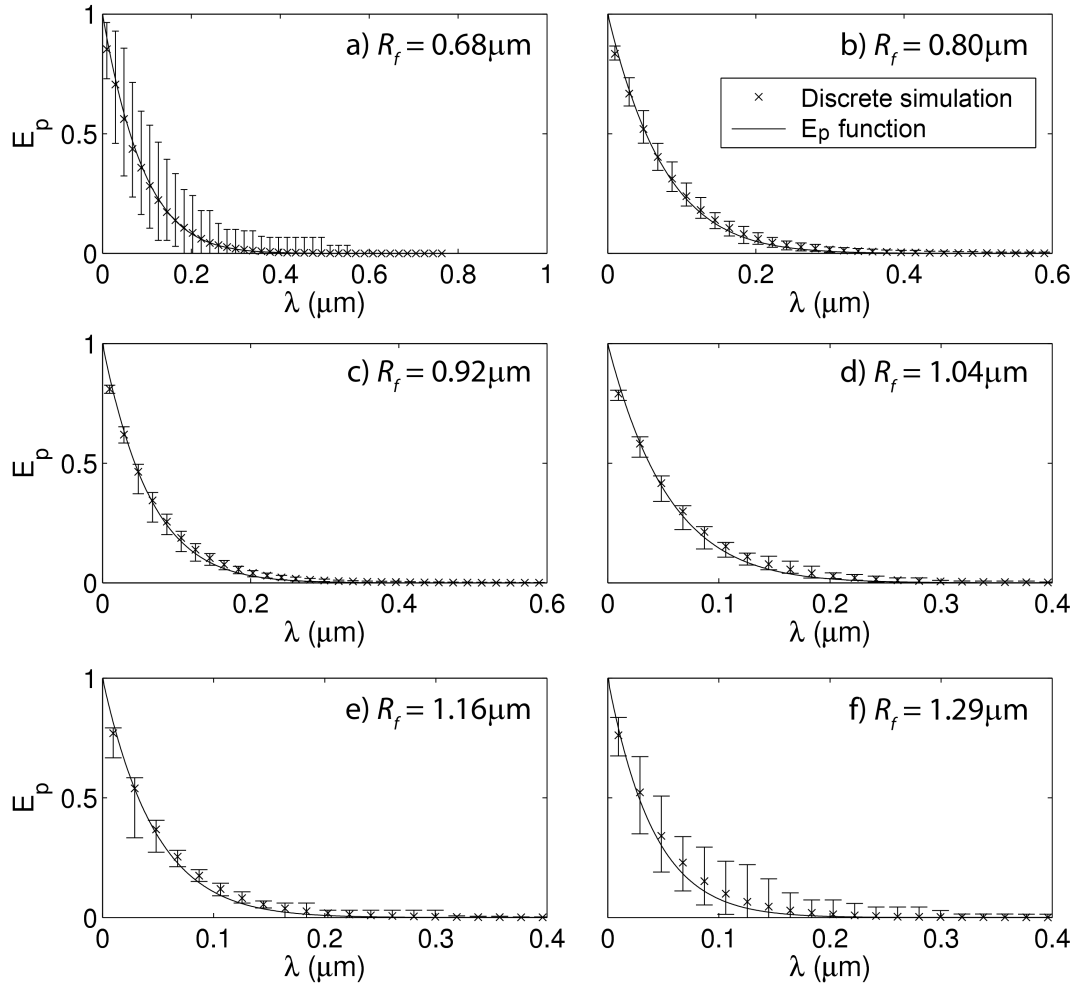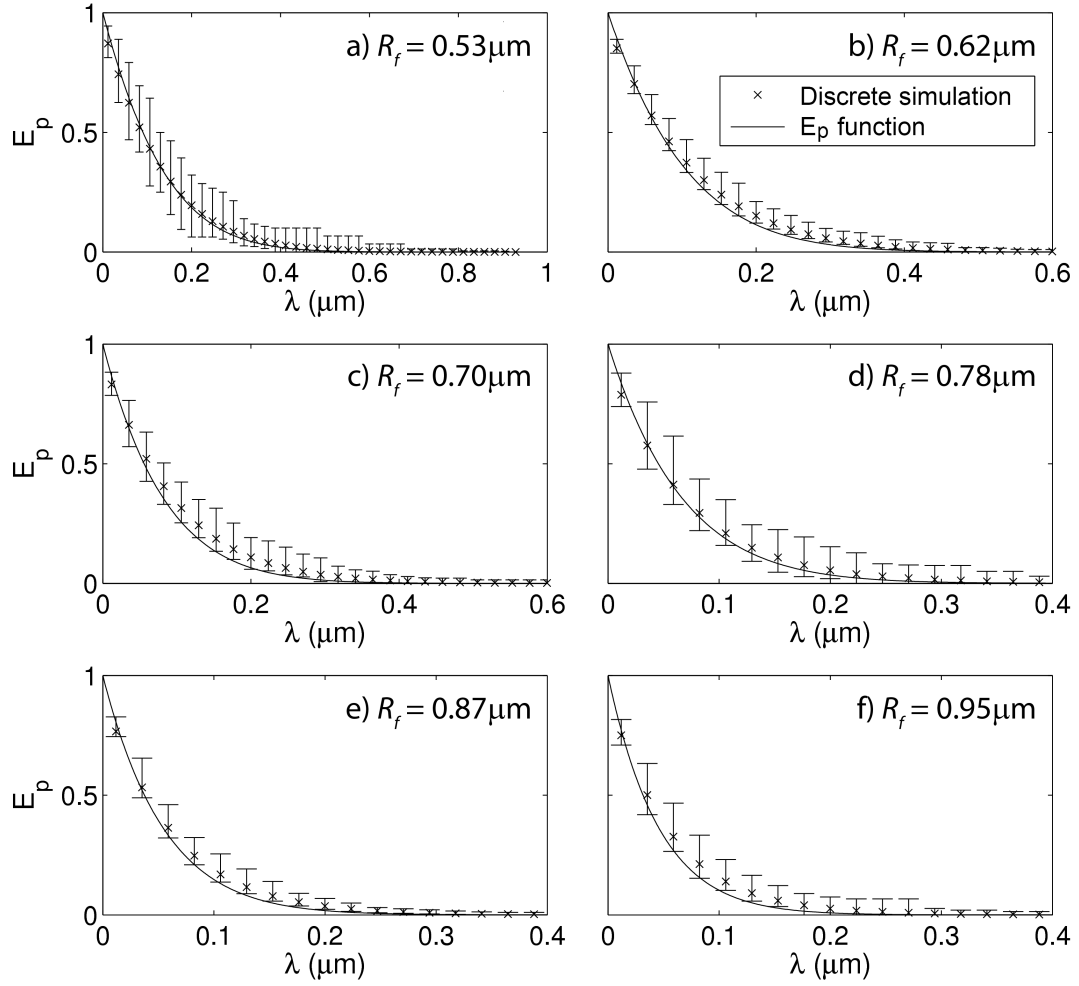
Figure 7: A comparison of the predicted exclusion probability and the exclusion probability measured from a bimodal distribution of particles created numerically. The black crosses refer to the numerically generated data whilst the red line describes the prediction.

needs to be extended to account for the size of the neighbouring particles. Figure 1 illustrates the difference between the $H_p(\lambda^*, R)$ and $G_p(\lambda^*, R, R_2)$ functions. In Figure 1 (b), the $G_p(\lambda^*, R, R_2)$ function describes the domain Ω originating from the reference particle's centre to the nearest particle of radius greater than R_2. In this case, the $G_p(\lambda^*, R, R_2)$ function is a conditional probability of finding a spherical domain Ω free of neighbouring particles of radius greater than R_2. The $G_p(\lambda^*, R, R_2)$ is obtained from $H_p(R, \lambda^*)$ as describe by Torquato [25], with the moments that enter the calculation obtained from Equation set (24). Note that the integral is over the interval $[R_2, \infty]$. The $G_p(\lambda^*, R, R_2)$ function is given by Equation set (25).

$$\langle R^D(t) \rangle = \int_{R_2}^{\infty} R^D f(R, t)\, dR$$

$$N_v(t) = \int_{R_2}^{\infty} F(R, t)\, dR \tag{24}$$

$$\phi(t) = \frac{4\pi}{3} \int_{R_2}^{\infty} R^3 F(R, t)\, dR$$

$$x = \lambda^* / (2\langle R \rangle)$$

$$e_v(x) = \phi . exp\left[-2\phi S \left(a_0 x^3 + a_1 x^2 + a_2 x \right) \right]$$

$$e_p(x) = \frac{e_v(x)}{e_v(x = R/(2\langle R \rangle))} \tag{25}$$

$$G_p(x) = \frac{\phi S}{\langle D \rangle} \left(3a_0 x^2 + 2a_1 x + a_2 \right) e_p(x)$$

Figure 8 compares the predicted particle spacings and numerical measurements for the bimodal particle radius distributions for three different sizes of R_2. The calculation captures the correct behaviour however, there are noticeable discrepancies between the estimated values for λ from the discrete particle dispersion model and the $G_p(\lambda^*, R, R_2)$ function. Let the relative deviation be given by $d(R_1, R_2) = (\lambda_{G_p} - \lambda_r)/\lambda_r$, where λ_{G_p} and λ_r are the spacings obtained from $G_p(\lambda^*, R, R_2)$ and the discrete simulation, respectively. The average value for d is -0.16 $\pm$ 0.158 with a lower and upper limit of -0.41 and 0.25, respectively.

3. Numerical implementation

3.1. The particle growth rate

This work utilises the particle growth rate expression proposed by Svoboda *et. al.* [8], which is based on a multi-component description of diffusion in an alloy containing n many alloying elements. Let the chemical potential and concentration of the *ith* alloying element within the particle phase be given by μ_{ki} and c_{ki}, respectively. Similarly for the matrix phase, these are μ_{0i} and c_{0i}. The matrix diffusivity of the *ith* element is given by D_{0i}. The multi-component
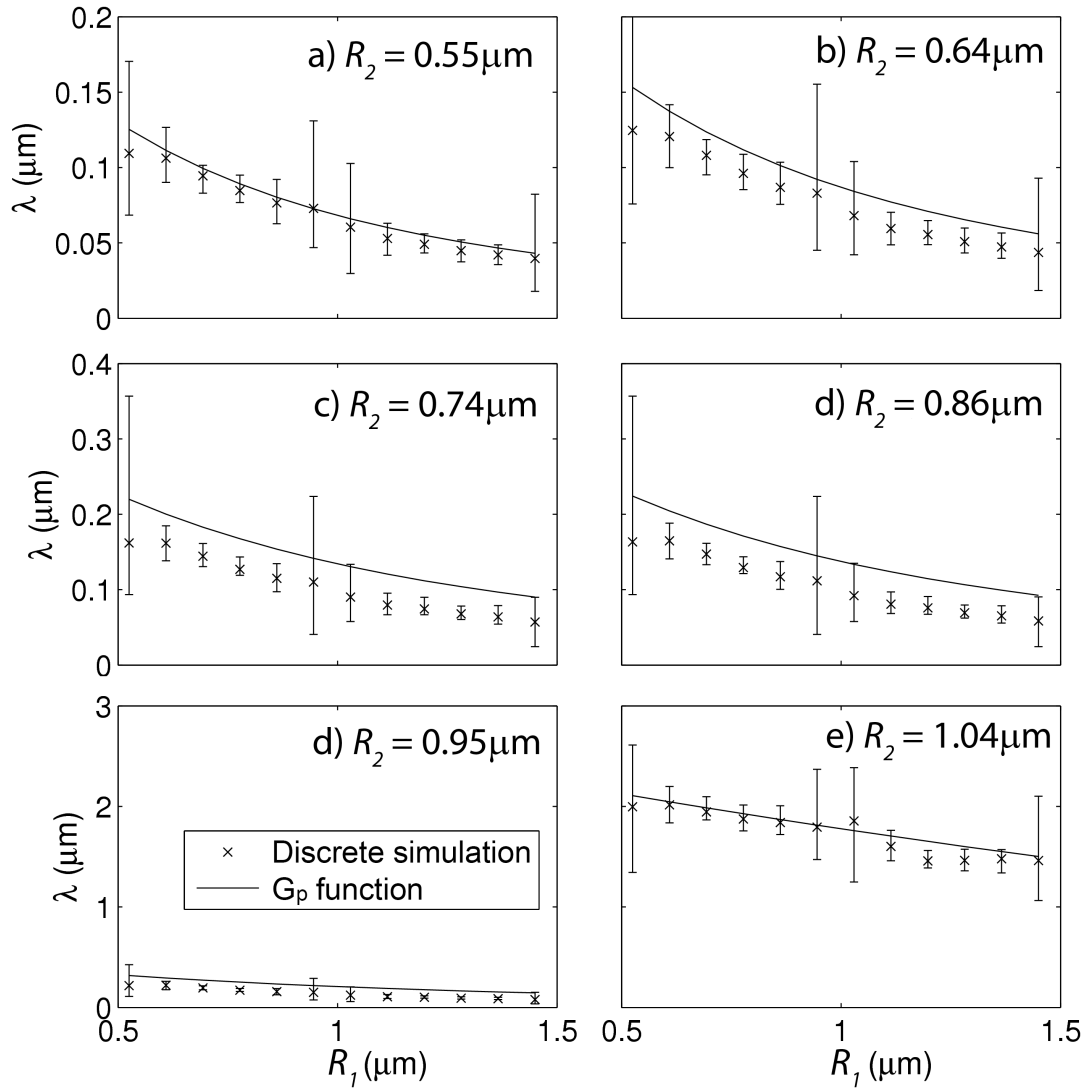
Figure 8: A comparison of the predicted and measured exclusion probability from a bimodal distribution of particles generated numerically.

growth rate of Svoboda *et. al.* [8] has been rearranged to have the same form as Equation (7). The terms A and R_c for this case are given below:

$$A = \frac{2\sigma}{R_g T} \left[\sum_{i=1}^{n} \frac{(c_{ki} - c_{0i})^2}{c_{0i} D_{0i}} \right]^{-1} \tag{26}$$

$$R_c = \frac{2\sigma}{-U_{mis} - \sum_{i=1}^{n} c_{ki}(\mu_{ki} - \mu_{0i})} \tag{27}$$

where σ is the interfacial energy, U_{mis} is the misfit strain energy, T is the absolute temperature and R_g is the gas constant. For non-dilute particle dispersions, Marqusee and Ross [14] introduced the following correction factor for the particle growth rate

$$z(R, t) = 1 + R(t)\sqrt{4\pi N_v(t) \langle R(t) \rangle} \tag{28}$$

The model has been applied to describe the coarsening and coalescence kinetics of the γ' phase particles in the nickel-based superalloy, Inconel 738LC. This alloy contains a high volume fraction of particles in the as-heat treated condition, making it suitable for the proposed calculations. The composition is given in Table 1. The commercial software Thermocalc [10] has been used to calculate the thermodynamic and mobility parameters, making use of the thermodynamic database TTNI8 and mobility database MOBNi1.

Al	B	C	Co	Cr	Mo	Nb	Ni	Ta	Ti	W	Zr
7.26	0.05	0.52	8.19	17.5	1.04	0.513	bal	0.549	4.09	0.803	0.0342

Table 1: Chemical composition of IN738LC (at.%)

3.2. Normalisation and reformulation

The normalisation procedure outlined by Lifshitz and Slyozov [2] has been applied to the coalescence source and sink rates. The spatial and temporal terms are now made dimensionless with the normalisation constants R_k and τ, respectively. The normalised continuity equation is given by

$$\frac{\partial \xi(r, t')}{\partial t'} + \frac{\partial \xi(r, t')v(r, t')}{\partial r} = q^+(r, t') - q^-(r, t') \tag{29}$$

15

where the normalised coalescence source and sink are given by q^+ and q^- respectively. The normalised model parameters are defined as

$$\xi(r,t')dr \equiv F(R,t)R_k^3 dR \equiv \frac{3}{4\pi}\left(\frac{R_k}{R}\right)^3 g(R,t)dR$$

$$r \equiv R(t)/R_k$$

$$r_c \equiv R_c(t)/R_k$$

$$t' \equiv t/\tau \tag{30}$$

$$\lambda' \equiv \lambda^*(t)/R_k$$

$$\Gamma' \equiv \Gamma(R, R_2, \lambda^*)\tau$$

$$G_p' \equiv G_p(R, R_2, \lambda^*)R_k$$

$$\tau \equiv R_k^3/A(t)$$

The normalised moments are given by Equation set (31) with the normalised particle growth rate given in Equation (32). These have been obtained by substituting Equation (10) into Equations (13) and (14). The normalised coalescence source and sink rates are given in Equations (33) and (34), respectively.

$$N_v(t) = \frac{1}{R_k^3}\int_0^\infty \xi(r,t')\,dr = \frac{1}{R_k^3}n_v(t/\tau)$$

$$\langle R(t)\rangle = \frac{R_k}{n_v}\int_0^\infty r\xi(r,t')\,dr = R_k(t/\tau)\langle r\rangle \tag{31}$$

$$\phi(t) = \frac{4\pi}{3}\int_0^\infty r^3\xi(r,t')\,dr$$

$$v = \frac{1}{r}\left(\frac{1}{r_c(t/\tau)} - \frac{1}{r}\right)z(r,t/\tau) \tag{32}$$

$$q^+(r,t') = \frac{8\pi}{9}n_v(t')\int_0^\infty\int_0^\infty \frac{\xi((r^3-r_2^3)^{1/3},t')\xi(r_2,t')r_2^3\,r^2\,(r^3-r_2^3)}{(r^3-r_2'^3)^{2/3}}$$
$$\times\,G_p'\left((r^3-r_2^3)^{1/3},r_2',\lambda'\right)\Gamma'\left((r^3-r_2^3)^{1/3},r_2',\lambda'\right)\,dr_2'\,d\lambda' \quad (33)$$

$$q^-(r,t') = \frac{16\pi}{9}n_v(t')\int_0^\infty\int_0^\infty \xi(r,t')\,r^3\,\xi(r',t')\,r'^3\,G_p'(r,r',\lambda')\,\Gamma'(r,r',\lambda')\,dr'\,d\lambda' \tag{34}$$

Further improvement to the accuracy of the calculation may be obtained by describing the particle radius distribution in a space scaled by the volume of the particle, as shown below.

$$\gamma(r,t')dr \equiv \frac{4\pi}{3}\xi(r,t')r^3dr \tag{35}$$

This reformulation avoids loss of significance errors which may occur when there is a large difference between the mean particle sizes of multi-modal particle dispersions. This normalisation leads to the following form of the continuity equation

$$\frac{\partial\gamma(r,t')}{\partial t'} + \frac{\partial(\gamma(r,t')v(r,t'))}{\partial r} = \frac{3}{r}\gamma(r,t') + \omega^+(r,t') - \omega^-(r,t') \tag{36}$$

where $\omega^+(r, t')$ and $\omega^-(r, t')$ are the reformulated coalescence rates

$$\omega^+(r, t') = \frac{1}{2} n_v \int_0^\infty \int_0^\infty \frac{r^2 \, \gamma((r^3 - r_2^3)^{1/3}, t') \, \gamma(r_2, t')}{(r^3 - r_2'^3)^{2/3}}$$
$$\times G_p'((r^3 - r_2^3)^{1/3}, r_2, \lambda') \, \Gamma'((r^3 - r_2^3)^{1/3}, r_2, \lambda') \, d\lambda' \, dr_2 \quad (37)$$

$$\omega^-(r, t') = n_v \int_0^\infty \int_0^\infty \gamma(r, t') \, \gamma(r', t') \, G_p'(r, r', \lambda') \, \Gamma'(r, r', \lambda') \, d\lambda' \, dr_2 \quad (38)$$

The reformulated moments are obtained as follows

$$N_v(t) = \frac{3}{4\pi R_k^3} \int_0^\infty r^{-3} \, \gamma(r, t') \, dr$$

$$\langle R(t) \rangle = R_k \int_0^\infty r^{-2} \, \gamma(r, t') \, dr \bigg/ \int_0^\infty r^{-3} \, \gamma(r, t') dr \quad (39)$$

$$\phi(t) = \int_0^\infty \gamma(r, t') \, dr$$

3.3. Numerical considerations

The numerical methods described by Anderson et al [29] were applied to solve the continuity equation given in Equation 36. A Courant-Friedrichs-Lewy condition was used to determine the appropriate time step based upon the particle growth and coalescence rates.

When calculating the coalescence rate, the maximum spacing λ_m' for two particles sized R_1 and R_2 was calculated by determining the distance λ' such that $G_p(R_1, R_2, \lambda') \approx 0$. The distance $\lambda' = R_1$ to $\lambda' = \lambda_m'$ was then discretized and $G_p(R_1, R_2, \lambda')$ and $\Gamma(R_1, R_2, V, \lambda')$ calculated for these ordinates. The computation time was improved by first calculating the $G_p(F(R, t), R_1, R_2)$ coefficients as a function of R_2 to avoid repetition. A smaller number of ordinates was used to discretize the coalescence rates than used to define the particle radius distribution with cubic spline interpolation linking the discretizations.

4. Results

4.1. Particle coarsening and coalescence

Numerical solutions of Equation (36) for the unimodal and bimodal dispersions introduced in Section 2.3 (and shown Figure 3) will now be presented. The predicted evolution of these distributions are shown in Figure 9 for different values of the scaling parameter k introduced in Section 2.2. The corresponding mean particle radius $\langle R(t) \rangle$ and concentration $N_v(t)$ for these cases are shown in Figure 10. The condition of $k = 0$ is descriptive of kinetics entirely driven by Ostwald ripening without particle coalescence. In this limit, the mean particle radius of the unimodal particle dispersion is observed to decrease during the transient coarsening regime as shown in Figure 10 a). Figure 10 b) shows that approximately 1000h is needed for particles to shrink sufficiently to fully dissolve within the matrix, initiating the reduction of the particle

concentration. Particle coalescence changes this behaviour, causing the reduction in the particle number density prior to complete dissolution. As a result of coalescence, there is a brief increase in mean particle radius as shown in Figure 10 a). The impact of coalescence upon the evolution of the particle distribution is shown in Figure 9. A significant number of coalesce events result in the skewing of the size distribution to the right, as shown in Figure 9 b).

For the bimodal dispersion with $k = 0$, the simulated behaviour begins with the dissolution of the smaller population of particles to allow for the growth of the larger population. It takes approximately 500h for the smaller particle population to commence dissolution. During this time scale the mean particle radius decreases (see Figure 10(c)). As the small particles are removed from the system, the mean particle radius increases; however after 2000h the smaller particles have been completely dissolved and $\langle R \rangle$ decreases. To continue coarsening, competitive growth must occur between the larger population of particles. This results in a decreasing mean particle radius, as particles from the larger population start to shrink. Once these particles fully dissolve, the mean particle radius then continues to increase. By this time the particle dispersion is nearing the steady state coarsening regime, as shown in Figures 9 i) and j). These solutions illustrate that it can take a few hundred hours to establish steady state (regime were the mean particle size scales with $t^{1/3}$) for unimodal particle distribution and considerably longer for a bimodal dispersion.

Particle coalescence changes this behaviour for the bimodal distribution, introducing a new population of coalesced particles as shown in Figure 9 g). Such solutions arise from repeated coalescence events between the largest and smallest particle populations. The predicted series of events change so that after the first population of the bimodal particle dispersion dissolves, a multi-modal particle dispersion remains. For the condition where $k = 1/30$, a tri-modal particle population exists after 20,000h as shown in Figure 9 j).

4.2. Attractor states

The impact of coalescence upon the evolution of the unimodal and bimodal particle size distributions towards the attractor state has been studied. The attractor state is important in that once reached the moments of the particle size distribution follow simple scaling laws, i.e., $\langle R \rangle \sim t^{1/3}$. LSW derived an analytical solution to describe the attractor state in the limit of dilute particle dispersions. For non-zero volume fraction particle systems, analytical solutions are difficult to derive and in most cases obtained numerically. Chen and Voorhees [27] have investigated the impact of the initial shape of the particle size distribution on its evolution towards the attractor state using a phase space representation. This approach has been adopted in the present work.

The phase space is constructed from the temporal evolution of moments of the particle size
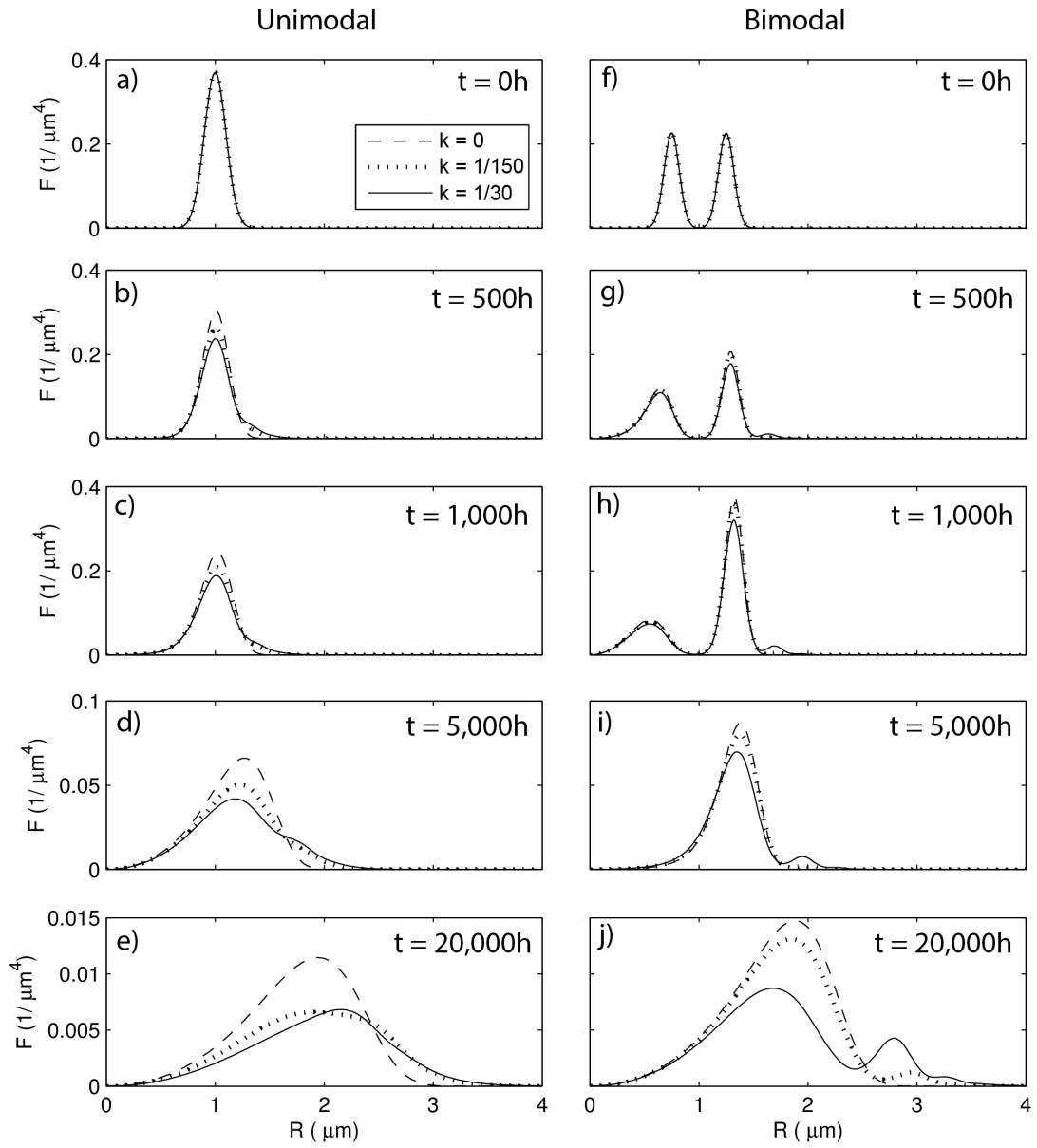
Figure 9: The simulated evolution of the particle radius distribution for different values of k.
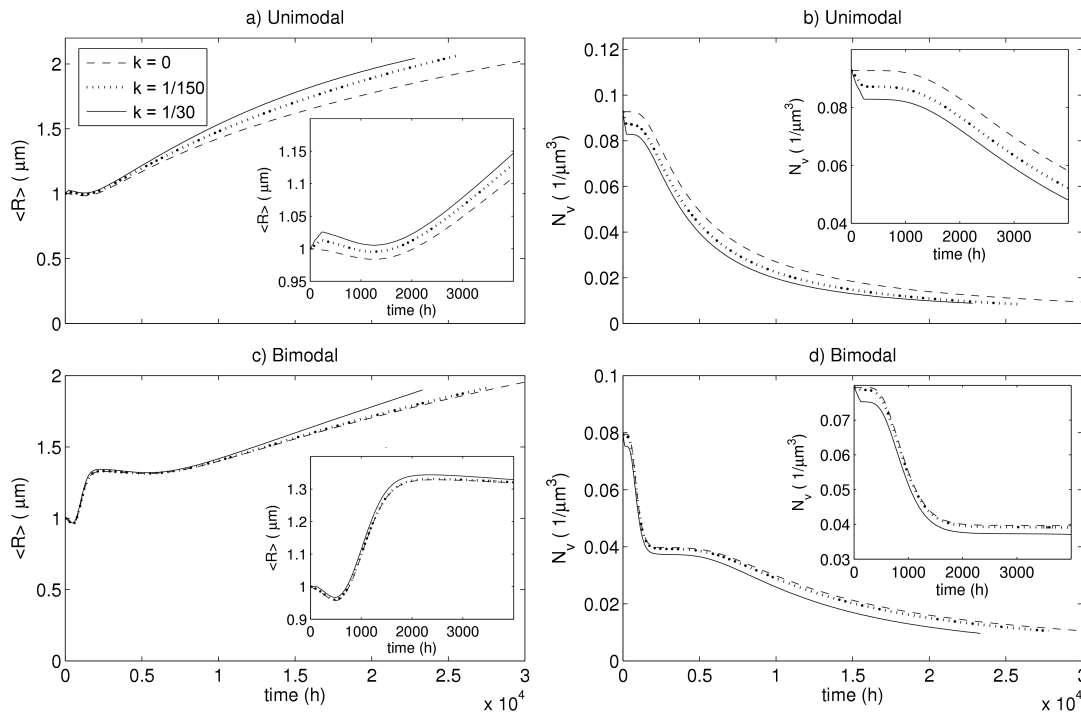
Figure 10: Statistical predictions of the coarsening kinetics of the bimodal and unimodal particle dispersions with different values of k

probability density function $\omega(\rho,t)$, where $\rho = R/\langle R \rangle$. The $\omega(\rho,t)$ distribution is related to $F(R,t)dR$ as follows

$$\omega(\rho,t)\,d\rho = \frac{1}{B\,\langle R \rangle}F(R,t)\,dR \qquad (40)$$

where B is an integration constant that ensures $\int_0^\infty \omega(\rho,t)\,d\rho = 1$. The n-th moments $h_n(t)$ of $\omega(\rho,t)$ with respect to ρ are given by

$$h_n(t) = \int_0^\infty \rho^n \omega(\rho,t)d\rho \qquad (41)$$

A trajectory in phase space is given by the pair $\left(h_n(t), \dot{h}_n(t)\right)$.

Following Chen and Voorhees [27], the attractor state for particle dispersions containing volume fractions of 1% , 20% and 40% have been calculated and are shown in see Figure 11. These were calculated using the $z(R,t)$ factor derived by Marqusee and Ross [14]. The simulated evolution of $\omega(\rho,t)$ for the unimodal and bimodal particle dispersions are shown in Figure 12, for different magnitudes of k. For the unimodal dispersion, particle coalescence increases the right hand tail of $\omega(\rho,t)$, as shown in Figure 12 a) to e). The coalescence behaviour for the bimodal dispersion is such that distinct new populations of coalesced particles are formed, as shown in Figure 12 j). Figures 13 e) and 14 e) show the trajectories in phase space for the unimodal and bimodal particle dispersions, plotting h_2 against dh_2/dt. The 2nd moment of $\omega(\rho,t)$ is descriptive of the width of the distribution. The direction of the trajectory is given by arrows with
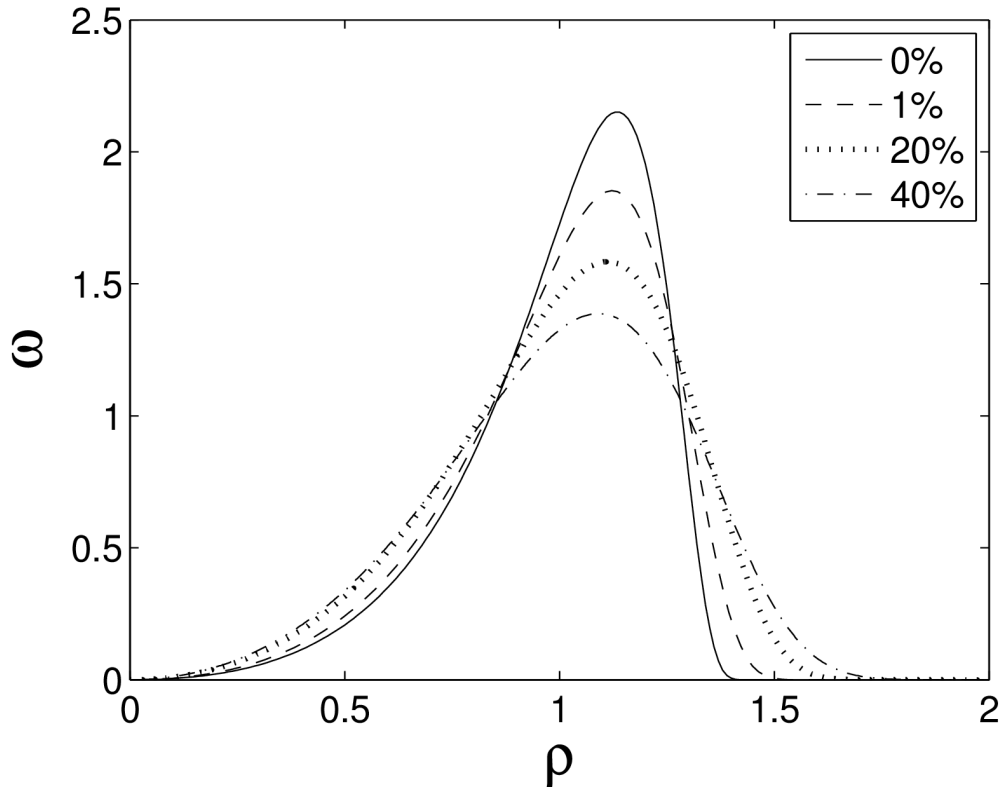
Figure 11: The attractor shapes based on the Marqusee and Ross [14] z factor.

dispersions at select times shown in the Figures a), b), c) and d).

For the unimodal particle dispersion with $k = 0$, the initial width of the dispersion is less than that of the distribution at steady state. The results from $k = 1/30$ and $k = 1/150$ show a much larger increase in width, with the trajectory curling around towards that of $k = 0$. The initial increase in h_2 for $k = 1/30$ and $k = 1/150$ is due to widening of the distribution resulting from coalescence forming a large tail on the right hand side of the dispersion at the beginning of the simulation. The bimodal trajectory for $k = 0$ starts with a lower value for h_2 than the attractor state. The moment h_2 increases as the smaller population of particles shrink and the larger population grows. As the smaller population of particle is removed, the width of the dispersion narrows. The larger population then proceeds to widen, as it coarsens towards the attractor state. Similar to the behaviour of the unimodal coarsening kinetics, particle coalescence results in an initial increase in h_2 due to the formation of a population of coalesced particles. The presence of the coalesced particles results in an offset in the value of h_2 compared to the results from $k = 0$.
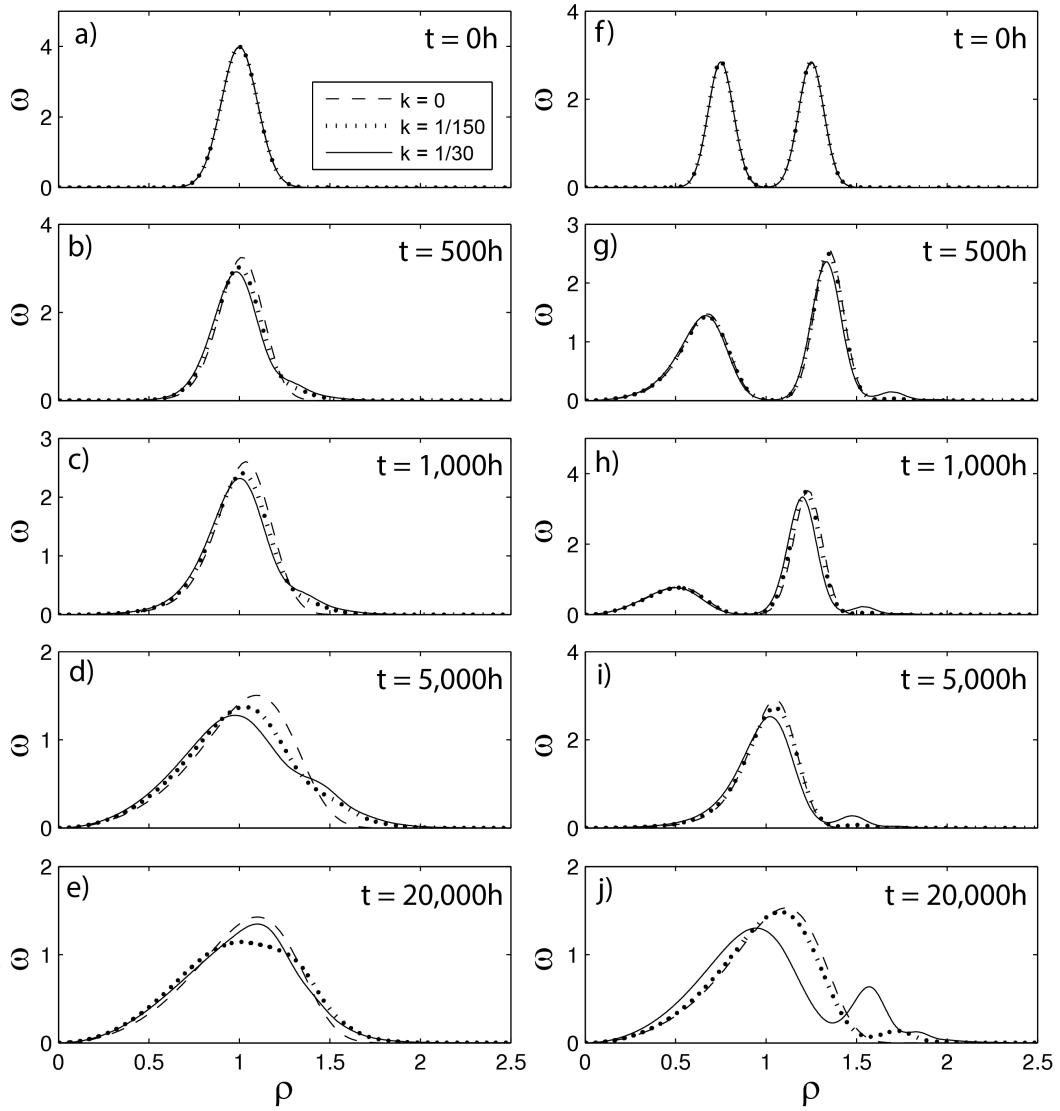
Figure 12: The evolution of the particle distribution shape for the unimodal and bimodal particle dispersions.
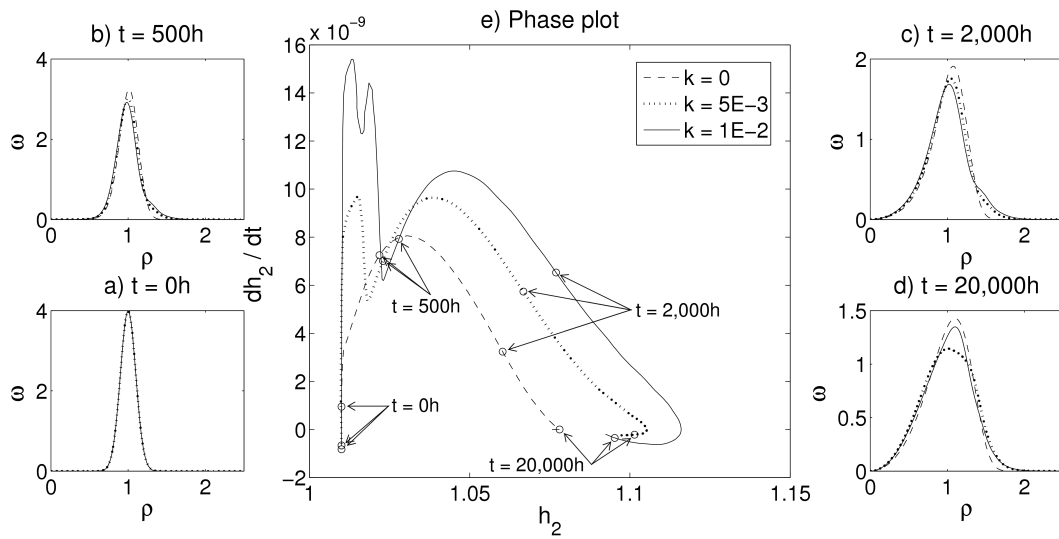
Figure 13: A phase plot of the trajectory of the unimodal particle dispersion during coarsening
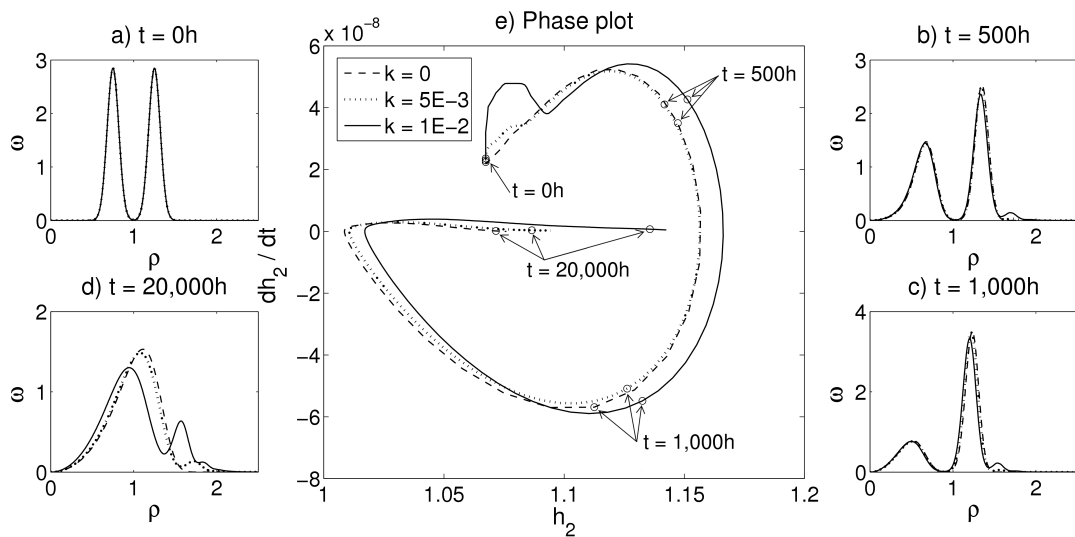

Figure 14: A phase plot of the trajectory of the bimodal particle dispersion during coarsening

5. Discussion

The present work has focused on modelling the influence of particle coalescence events on Oswald ripening. The coalescence rates were determined using of nearest neighbour functions to capture the spatial arrangement of the particle dispersion. The model has been applied to a unimodal and bimodal particle size distributions. Numerical solution of Equation (36) with a starting unimodal dispersion predicts that particle coalescence has the effect of skewing the particle radius distribution to the right, i.e., the density of the large particles is increased (see Figure 12). For the bimodal distribution, the proposed model predicts new distinct particle populations when coalescence takes place, as shown in Figure 9 j).

Particle coalescence extends the transient coarsening regime, as well as, perturbing the trajectory towards the attractor state, as shown in Figures 13 and 14. The numerical solution presented in this study were upto 20,000h, and within this time frame the unimodal dispersion reached the attractor state but the bimodal did not. As the particle dispersion coarsens, the spacing increases and the particle concentration decreases, slowing the rate of coalescence. As the impact of particle coalescence reduces, Ostwald ripening kinetics becomes the dominate mechanism, with the dispersion evolving towards the Ostwald ripening attractor state.

Many alloys are specifically heat treated to obtain particle dispersions that evolve within the transient coarsening regime. This work has shown that particle coalescence has a large impact upon this regime, deviating the trajectory from the steady state. Including the mechanism may prove important in capturing particle kinetics in greater detail.

A key limitation in the mean field description is the description of the particle geometry, where complex morphologies are approximated by a sphere of equivalent volume. The parameter k was introduced to address the deviation of the growth of particles with complex morphologies that have non-uniform curvature, and thus non-uniform growth rates, from that expected from spherical particles. Kozeschnik *et al.* [30] used shape factors to describe the particle growth rate of disc or needle shaped precipitates. A similar approach could use to determine the k parameter. Alternatively, the evolution of the shape factor could be derived in the context of energy minimisation to determine particle morphology that accounts for coalescence events. Determining the energy minimising geometry within a non-dilute particle dispersion is a non-trivial task, as the energy minimising shape is often sensitive to the local spatial arrangement of particles due to the overlapping of strain fields between neighbouring precipitates [21].

Another consideration is the description of the chemical composition of the precipitates. The composition of the particle phase is currently described by mean values. Significant differences in chemistry between particle populations of γ' particles in Nickel based superalloys has been

24

observed [31]. The difference in composition would affect chemical potentials and thus particle growth rates, impacting the continued growth behaviour of coalesced particles. The accuracy of the calculation may be improved by accounting for such differences, however such detail comes at the expense of increased computation time due to the increased number of combinations of particles of different compositions that would need to be assessed.

6. Conclusions

An extension to a mean field description of particle coarsening to include coalescence has been presented. This has been achieved through the introduction of source and sink terms associated with particle amalgamation into the population dynamics equation governing the evolution of the particle radius distribution. Nearest neighbour functions have been used to characterise the spatial distribution of particles and these were used to estimate the frequency of coalescence. The particle growth rates were determined using the multi-component relation for the particle interface velocity developed by Svoboda *et al.* [8] which also accounts for misfit stresses.

The accuracy of nearest neighbour functions used to describe the spatial statistics of a dispersion has been assessed against a numerically generated discrete ensemble of particle in three dimensions. It is demonstrated that the nearest neighbour function and the discrete particle model are in good agreement when describing interparticle spacing. They reproduce the observed behaviour in which large particles have smaller spacings to the nearest neighbouring particle and greater probability of having a small particle as the nearest neighbour. This is more pronounced for multi-modal particle dispersions.

Numerical studies of the trajectories in phase space of an initial unimodal and bimodal dispersion have been carried out. The paths followed by these distributions are shown to be distinctly different (see Figures 13 and 14). It is demonstrated that the inclusion of particle coalescence influences the time scales to reach the attractor state.

References

[1] G. W. Greenwood, The growth of dispersed precipitates in solutions, Acta. Metall. 4 (3) (1956) 243 − 248.

[2] I. M. Lifshitz, V. V. Slyozov, The kinetics of precipitation from supersaturated solid solutions, J. Phys. Chem. Solids. 19 (1961) 35–50.

[3] C. Z. Wagner, Theorie der Alterung von Niederschlagen durch Umlonsen (Ostwald-reifung), Z. Elektrochem 65 (1961) 581–591.

[4] X. Li, N. Saunders, A. P. Miodownik, The coarsening kinetics of γ' particles in nickel-based alloys, Metall. Mater. Trans. A 33 (11) (2002) 3367–3373.

[5] C. J. Kuehmann, P. W. Voorhees, Ostwald ripening in ternary alloys, Metall. Mater. Trans. A 27 (1996) 937–943.

[6] H. J. Jou, P. W. Voorhees, G. B. Olson, Computer simulations for the prediction of microstructure/property variation in aeroturbine disks, in: Green, KA *et. al.* (Ed.), Superalloys 2004, 2004, pp. 877–886.

[7] T. Philippe, P. W. Voorhees, Ostwald ripening in multicomponent alloys, Acta. Mater. 61 (11) (2013) 4239–4244.

[8] J. Svoboda, F. D. Fischer, P. Fratzl, E. Kozeschnik, Modelling of kinetics in multi-component multi-phase systems with spherical precipitates: I: Theory, Mat. Sci. Eng. A-Struct. 385 (2004) 166–174.

[9] Q. Chen, J. Jeppsson, J. Agren, Analytical treatment of diffusion during precipitate growth in multicomponent systems, Acta. Mater. 56 (8) (2008) 1890–1896.

[10] J. Andersson, T. Helander, L. HÃűglund, P. F. Shi, B. Sundman, THERMO-CALC & DICTRA, computational tools for materials science, CALPHAD 26 (2) (2002) 273–312.

[11] J. Svoboda, F. D. Fischer, P. Fratzl, E. Kozeschnik, The scientific tool box for enjoyable computational materials engineering@ONLINE (2015).
URL http://matcalc.tuwien.ac.at/

[12] A. J. Ardell, The effect of volume fraction on particle coarsening: theoretical considerations, Acta. Metall. Mater. 20 (1) (1972) 61 − 71.

[13] P. W. Voorhees, M. E. Glicksman, Solution to the multi-particle diffusion problem with applications to Ostwald Ripening. 1. Theory, Acta. Metall. Mater. 32 (11) (1984) 2001–2011.

[14] J. A. Marqusee, J. Ross, Theory of Ostwald ripening - competitive growth and its dependence on volume fraction, J. Chem. Phys. 80 (1984) 563–543.

[15] H. Hayakawa, F. Family, Many-body effects in 2-dimensional Ostwald ripening, Physica A 163 (2) (1990) 491–500.

[16] K. Tsumuraya, Y. Miyata, Coarsening models incorporating both diffusion geometry and volume fraction of particles, Acta. Metall. Mater. 31 (3) (1983) 437–452.

[17] K. G. Wang, M. E. Glicksman, K. Rajan, Length scales in phase coarsening: Theory, simulation, and experiment, Comp. Mater. Sci. 34 (3) (2005) 235–253.

[18] J. Svoboda, F. Fischer, Generalization of the lifshitz-slyozov-wagner coarsening theory to non dilute multi-component systems, Acta. Mater. 79 (0) (2014) 304 − 314.

[19] M. Doi, Coarsening behaviour of coherent precipitates in elastically constrained systems, Mater. T. JIM 33 (7) (1992) 637–649.

[20] P. W. Voorhees, G. B. McFadden, W. C. Johnson, On the morphological development of 2nd phase particles in elastically-stressed solid, Acta. Metall. Mater. 40 (11) (1992) 2979–2992.

[21] C. H. Su, P. W. Voorhees, The dynamics of precipitate evolution in elastically stressed solids - i. inverse coarsening, Acta. Mater. 44 (5) (1996) 1987 − 1999.

[22] C. K. L. Davies, P. Nash, R. N. Stevens, Effect of volume fraction of precipitate on Ostwald ripening, Acta. Mater. 28 (2) (1980) 179–189.

[23] R. N. Stevens, C. K. L. Davies, The unique attractor in the theory of Ostwald ripening, Scripta. Mater. 46 (1) (2002) 19–23.

[24] B. L. Lu, S. Torquato, Nearest-surface distribution-functions for polydispersed particle-systems, Phys. Rev. A 45 (8) (1992) 5530–5544.

[25] S. Torquato, Random Heterogeneous Materials: Microstructure and Macroscopic Properties, Interdisciplinary Applied Mathematics, Springer New York, 2013.

[26] N. F. Carhnahan, K. E. Starling, Equation of state for nonattracting rigid spheres, J. Chem. Phys. 51 (2) (1969) 635− 636.

[27] M. K. Chen, P. W. Voorhees, The dynamics of transient Ostwald Ripening, Model. Simul. Mater. Sci. Eng. 1 (1993) 591–612.

[28] J. Zhou, Y. Zhang, J. K. Chen, Numerical Simulation of Random Packing of Spherical Particles for Powder-Based Additive Manufacturing, J. Manuf. Sci. Eng. 131 (3).

[29] M. J. Anderson, A. Rowe, J. Wells, H. C. Basoalto, Application of a multi-component mean field model to the coarsening behaviour of a nickel-based superalloy, Acta. Mater. 114 (2016) 80 − 96.

[30] E. Kozeschnik, J. Svoboda, F. D. Fischer, Shape factors in modeling of precipitation, Mater. Sci. Eng. A 441 (1-2) (2006) 68–72.

[31] Y. Q. Chen, T. J. A. Slater, E. A. Lewis, E. M. Francis, M. G. Burke, M. Preuss, S. J. Haigh, Measurement of size-dependent composition variations for gamma prime (γ') precipitates in an advanced nickel-based superalloy, Ultramicroscopy 144 (2014) 1–8.